ICT Project No 871813
MUNDFAB
Modeling Unconventional Nanoscaled
Device FABrication

D2.4: Final experimental results on heated implants and SPER

P.L. Julliard (STM/CNRS), R. Monflier (CNRS),
R. Daubriac (CNRS), R. Démoulin (CNRS),
A. Hémeryck (CNRS), F. Cristiano (CNRS),
S. Kerdilès (LETI), M. Opprecht (LETI),
B. Sklénard (LETI), P. Michalowski (L-IMIF),
A. La Magna (CNR-IMM), M. Italia (CNR-IMM),
S. Mundinar (FhG-IISB),
A. Johnsson (FhG-IISB), P. Pichler (FhG-IISB)

26/02/2023

Quality management

This deliverable was reviewed by:

Dominic WALDHOER, TUW

Nicolas GUITARD, STM

Contents

Introduction

In this deliverable, we report the final results of our investigations about the impact of the wafer temperature on the residual damage remaining after an ion implantation process, as well as on the electrical activation of the implanted dopants.

In section 1, we will present the case of a "heated implant" of arsenic in silicon. The initial results already reported in Deliverable 2.1 will be expanded by new TEM and photoluminescence experiments and further analyzed with the help of dedicated Kinetic Monte Carlo (KMC) simulations.

In the second section, we will present the results obtained from dedicated SiGe wafers fabricated and laser annealed by CEA-LETI, specifically designed for tasks T2.1 and T2.2 of the project. These wafers were characterized by several techniques available at CEA-LETI, L-IMIF, CNR-IMM and CNRS-LAAS, allowing a comprehensive understanding of the different mechanisms responsible for damage recovery and dopant activation in sub-melt laser annealing conditions.

1   Complementary results for As HT-implants in Si

1.1 Wafers description and summary of previous results

The heated arsenic implantations were described in Deliverable 2.1 (https://www.mundfab.eu/content/dam/iisb/mundfab/documents/public-deliverables/2021-09-29-mundfab-d21-as-submitted.pdf). Three wafers were implanted at RT, 150°C and 500°C respectively, the details of the implantations are given in Table 1. These As implantations were followed by an identical annealing process, the details are given in Table 2.

Table 1 : Implantation conditions for As heated implants. The implantation is carried out in two steps, each step having a different energy and implantation dose.

Doping	Energy (keV)	Dose (cm^{-2})	Implant temperature	Annealing
As	180+100	1^E14+8^E13	RT	Table 2
As	180+100	1^E14+8^E13	150°C	Table 2
As	180+100	1^E14+8^E13	500°C	Table 2

Table 2 : Annealing process following the As heated implantations

	Temperature	Duration
Annealing 1	625°C	2h
Annealing 2	750°C	1h
Annealing 3	700°C	3h30
Annealing 4	625°C	52min
Annealing 5	800°C	30min
Annealing 6	750°C	1h

As-implanted and post-annealed TEM analyses were also performed on these wafers. As-implanted TEM cross-sectional images revealed the formation of an amorphous layer only in the RT implant case. After annealing, extended defects were observed in all three cases. For the RT and 150°C implantation cases, dislocation loops (DLs) were identified while for the 500°C case, (311) defects were found (Figure 1).
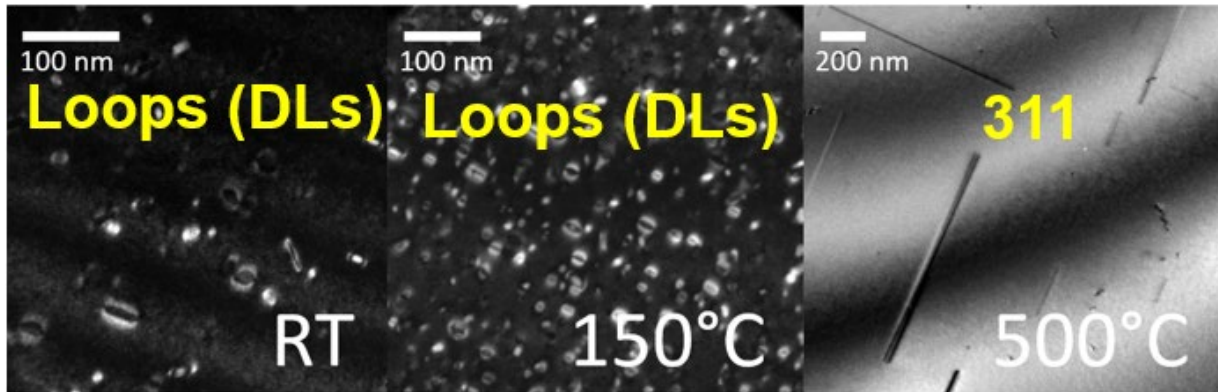

Figure 1: TEM plane-view of the three As implanted wafers after the annealing process

More recently, low temperature photoluminescence spectra were obtained on all three wafers after annealing (Figure 2) in order to identify defects present thanks to their optical emission properties occurring during the de-excitation of the material after electronic excitation. Several defect peaks were identified in these spectra.
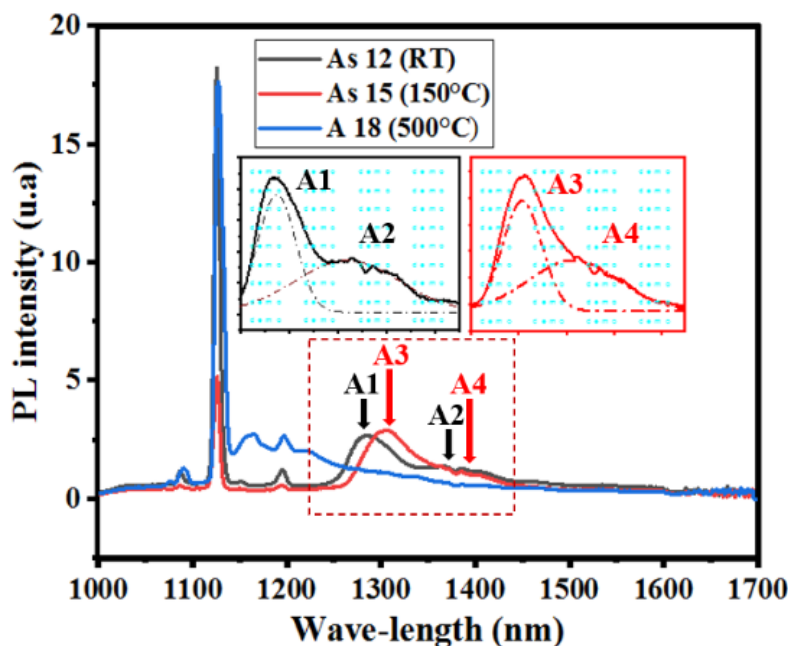

Figure 2: Photoluminescence spectrum of the three As implanted wafers after the annealing process where characteristic peaks A1, A2, A3 and A4 are observed.

Based on the TEM images presented in Deliverable D2.1, a count of interstitials trapped in the defects was performed for each implantation condition (RT, 150°C and 500°C implantations) (see also Table 3, page 8). By measuring the size of DLs and 311 defects and depending on the diffraction angle used in TEM, it is indeed possible the average number of interstitial trapped in these defects [1] (by counting the average number of interstitials per image, the density of interstitials trapped in these defects can be calculated).The interstitial count in the

dislocation loops (RT, 150°C implantations) and in the {311} defects (500°C) allows to have a quantitative criterion to evaluate the reliability of the predictions of the KMC simulations. This will be further discussed in section 1.2.

Another issue presented in deliverable D2.1 was the identification of defects that cause spikes in the photoluminescence spectra. For the processes involving RT and 150°C implantations, a similar photoluminescence signal was observed and two peaks near 1300 nm and 1350 nm, named A1-A2 for RT implantation and A3-A4 for 150°C implantation respectively were visible and discussed in deliverable D2.1. These peaks were assumed to be due to the same defect. In the rest of the deliverable, the peak at 1300 nm (A1 for RT and A3 for 150°C implant) will be referred to as A1 and the peak near 1350 nm (A2 for RT implant and A4 for 150°C implant) will be referred to as A2. These peaks were compared to those found in the literature for different types of defects generated by ion implantation followed by annealing. The peaks closest to those observed in our spectra are those noted I1 and I2 in [2] (and S1 and S2 in [3]). These peaks have been associated with interstitial clusters after Si implantations in silicon followed by annealing at limited temperatures (600°C in [2] and [3]). Such clusters may be too small to be observed in TEM. Another difficulty in identifying the peaks is that in [2] and [3] the peaks were associated with the stress field induced by the clusters and not with the clusters themselves.

1.2 Simulation strategy and new experiments

First, continuous and KMC simulations were performed to determine if the implantations followed by the annealing process could form such interstitial clusters. The continuous simulations do not predict a sufficiently high concentration of interstitial clusters to be consistent with the observed photoluminescence after the annealing process for all three implantation temperatures (not shown). The interstitials remaining after annealing are mainly in the DLs in the continuous simulations. The predictions of the KMC simulations are in agreement with the continuous simulations and will be discussed in detail in the next section. Another hypothesis to explain the A1 and A2 peaks would be that they are induced by the presence of DLs. The A1 and A2 peaks are indeed correlated with the presence of DLs in the TEM images. The broad shape of the A1 and A2 peaks suggests that in this case the peaks are more related to the stress field induced by the DLs than by the DLs themselves, as it is the case for the interstitial clusters discussed in [2] [3].

To help identify and distinguish the observed peaks, an additional annealing was therefore performed for the samples on the three wafers: they were annealed for 30 minutes at 700°C, 800°C, 900°C and 1000°C (resulting in 15 samples, including the reference sample without additional annealing). The purpose of these annealings is to follow the evolution of the photoluminescence spectra as a function of the temperature of the additional annealings applied. The photoluminescence spectra of wafers implanted at 150°C and 500°C are shown in Figure 3.
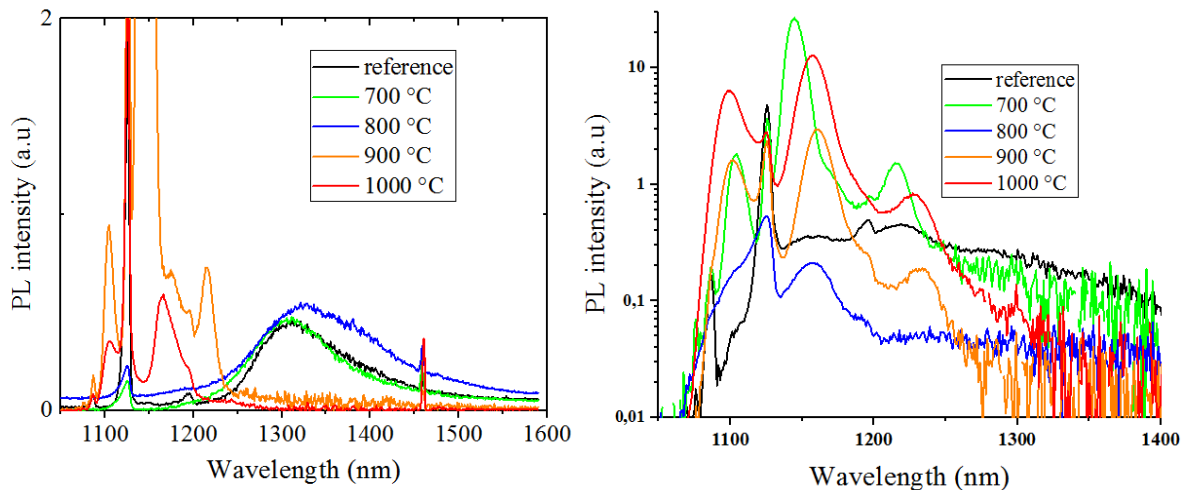
Figure 3: Photoluminescence spectra acquired at a temperature of 8K after additional annealing for 150°C implant (left) and 500°C implant (right). (The intensity scale is linear for the sample implanted at 150°C and logarithmic for the sample implanted at 500°C.)

➢ For the sample implanted at 150°C, additional annealing at 700°C and 800°C does not drastically change the photoluminescence peaks and the A1 and A2 peaks observed in Deliverable D2.1 are still visible. However, after additional annealing at 900°C, the peaks in the photoluminescence spectrum are different. The annealing at 900°C is therefore associated with an evolution of the defects responsible for the A1 and A2 peaks. In addition, new peaks appear between 1100 nm and 1250 nm for samples annealed at a temperature above 900°C.

Assuming that the A1 and A2 peaks are caused by the DLs observed in the TEM images, the defect change observed in the photoluminescence at 900°C should also be visible in the TEM images. Therefore, TEM analysis was performed on the wafer implanted at 150°C that were annealed at 800°C and 900°C. The plan-view TEM images of the samples without additional annealing, with annealing at 800°C and with annealing at 900°C are shown in Figure 4. For the three samples, DLs are observed in the TEM images. However, the density and size of the DLs are different depending on the additional annealing performed. For the 800°C annealing, the number of DLs visible in TEM is high and comparable to that found in the reference sample. For the sample annealed at 900°C, the number of DLs observed in the TEM image is much lower. The average size of the DLs appears to be larger in the case of the additional annealing at 900°C than in the reference case and the annealing at 800°C. The annealing at 900°C causes a change in the DLs observed in TEM. The TEM images are therefore consistent with the proposed link between the A1 and A2 peaks observed in photoluminescence and the presence of DLs. The reduction of the density of DLs and the increase of DL average size after the additional anneals is expected. The evolution of the DLs follows an Ostwald ripening [4] mechanism which favours the growth of the larger DLs while the smaller DLs disappear. The DLs observed in the reference sample as well as in the samples annealed at 800°C and 900°C are mostly faulted dislocations. The evolution of the stress field causing the A1 and A2 peaks would then be more related to the evolution of the density of DLs rather than to a change in the nature of the DLs.

The identification of the new peaks between 1100 nm and 1250 nm on the photoluminescence spectra of the sample annealed at 900°C is not explained at the moment and is under investigation.
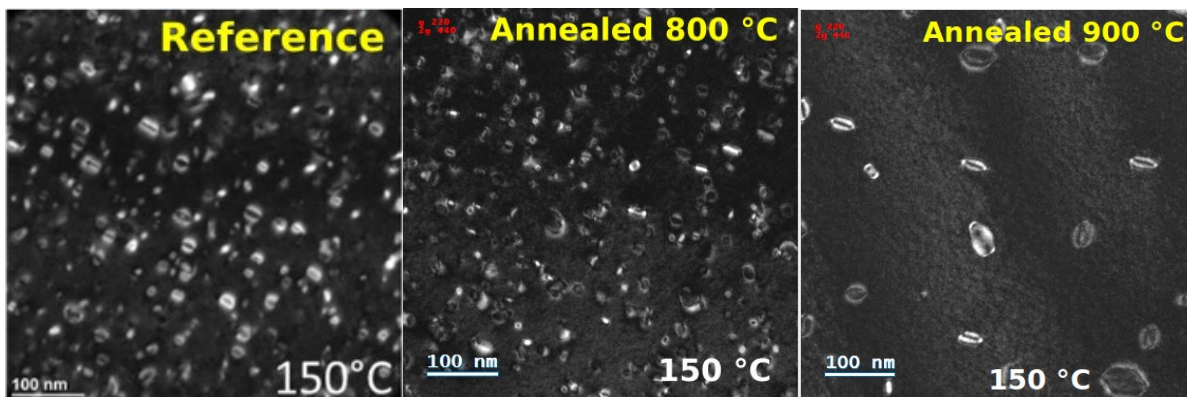

Figure 4: TEM plane view of the wafers implanted at 150°C without additional annealing (Left), with an additional annealing at 800°C 30 min (Middle) and with an additional annealing at 900°C 30 min (right).

➢ For implantation at 500°C the photoluminescence spectrum changes for any of the additional annealings performed. The defects responsible for the peaks observed in the reference sample are thus very sensitive to an additional annealing. Two peaks (around 1150 nm and 1230 nm) seem to be visible after most of the annealings performed (the peak at 1230 nm is always present except for the sample annealed at 800 °C). These two peaks appeared to be already present in the spectra of the sample without additional annealing in deliverable 2.1. A TEM analysis is planned to observe if the additional annealing at 700°C has an effect on the (311) defects observed in the reference sample. This study will conclude on the potential link between the (311) defects and the photoluminescence spectrum of the reference sample.

1.3 Status of KMC results

The three implantations followed by annealing were simulated using the KMC implemented in [5]. The KMC predictions regarding the as-implanted damage are in agreement with the TEM images presented in Deliverable D2.1. An amorphous layer is predicted in the case of the RT implantation. The absence of an amorphous layer observed in the TEM images for the 150°C and 500°C implantations is also well reproduced (Figure 5). The KMC is therefore a reliable tool to simulate the effect of implantation temperature on amorphization under these implantation conditions.
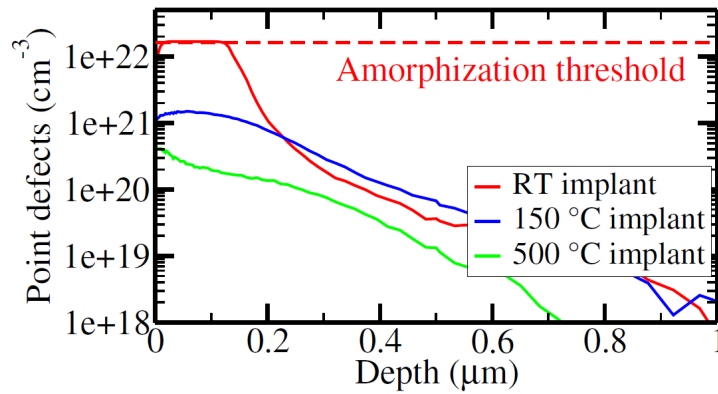
Figure 5: KMC simulation of point defects concentration as-implanted for the three As implantations. A dashed line indicates the point defect concentration threshold to form an amorphous material.

After annealing (Figure 6), the KMC predicts DLs in all three cases. The simulation is qualitatively consistent with TEM observations for the RT and 150°C implantation cases. On the other hand, the simulation fails to predict the (311) defects observed in the TEM images for the 500°C implantation case. The KMC does not distinguish between perfect and faulted DLs and therefore cannot be compared directly to the experimental results.
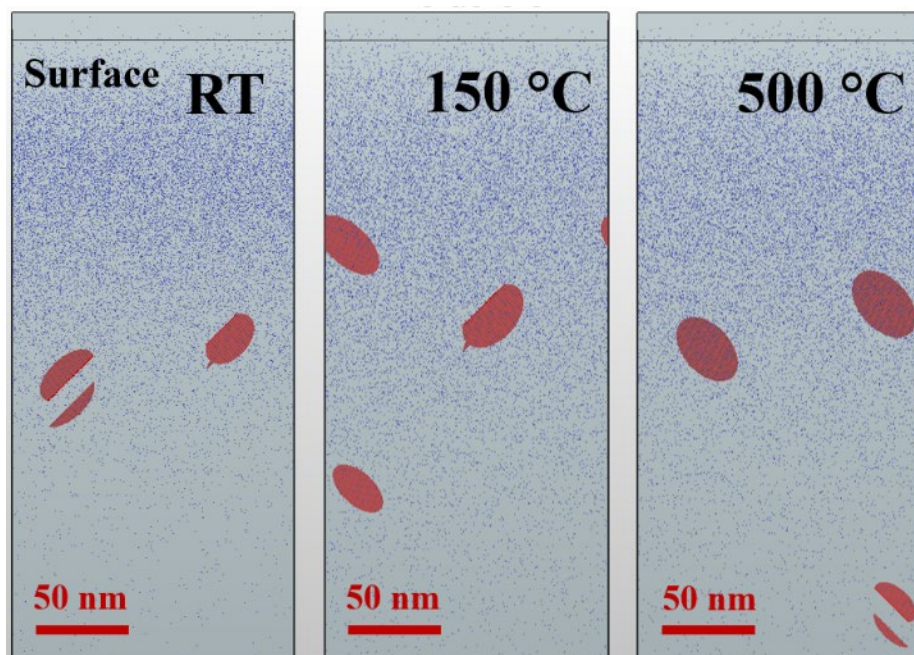

Figure 6: KMC simulations of the extended defects formed in depth after the annealing following the three As implantations in silicon and corresponding temperature. The red patches represent the DLs predicted by the KMC.

It is also possible to quantitatively compare the KMC with the experimental results using the density of interstitials trapped in the extended defects (DLs or (311) defects). For the RT and 150°C cases, the KMC predicts the same order of magnitude of interstitials trapped in the DLs. For the 500°C implantation, the density of interstitials trapped in the simulated DLs greatly overestimates the density of interstitials counted in the (311) defects in the TEM images. The KMC simulations thus appear to be reliable for the RT and 150°C implantations but fail to reproduce the experimental results for the 500°C implantation. The reasons for the differences between the predictions of the simulations and the experimental observations in this case will be discussed in Section 2.6

Table 3 : Density of trapped interstitials in extended defects (DLs or 311 defects) for the 3 As implantations.

	RT	150°C	500°C
TEM	$1.4 \cdot 10^{14}$ cm^{-2}	$1.6 \cdot 10^{14}$ cm^{-2}	$5.1 \cdot 10^{12}$ cm^{-2}
KMC	$1.4 \cdot 10^{14}$ cm^{-2}	$2.4 \cdot 10^{14}$ cm^{-2}	$1.9 \cdot 10^{14}$ cm^{-2}

Another limitation of KMC is the simulation time. In order to predict the occurrence of DLs, it is necessary to use large simulation boxes. The size of these boxes leads to a long simulation time especially for the simulation of the annealing process. The size of the simulation boxes (150 nm x 150nm surface) we used leads to a long simulation time (~48 hours).

Methods to overcome these two problems, (the reliability of the KMC for the 500°C implementation and the high simulation time) will be described in deliverable D2.6.

2. HT implants of B/P into Si & SiGe followed by nanosecond sub-melt laser annealing

2.1 Samples fabrication

Dedicated SiGe layers have been grown at CEA-Leti withinf WP3 (see deliverable D3.2). These wafers have been used to perform thermal implants (at room temperature, 150°C or 500°C) by AMAT. Afterwards, the wafers have been splitted into quadrants at CEA-Leti (see Figure 7.a). The details of the Design of Experiments (DoE) are shown in Figure 7.b. Explanations for the table and the choice for the laser energy values can be found in Deliverable D2.1 section 5. In the case of RT implants (wafers 1, 4, 7 and 10) two quarters of each wafer have been used to amorphize 15 or 30 nm (conditions labeled "Ge PAI 1" and "Ge PAI 2", respectively) in order to study the SPER using ns laser annealing (LA) (in the submelt regime) for Task T2.2 (See Sections 2.6 and 2.7).

(a)

(b)

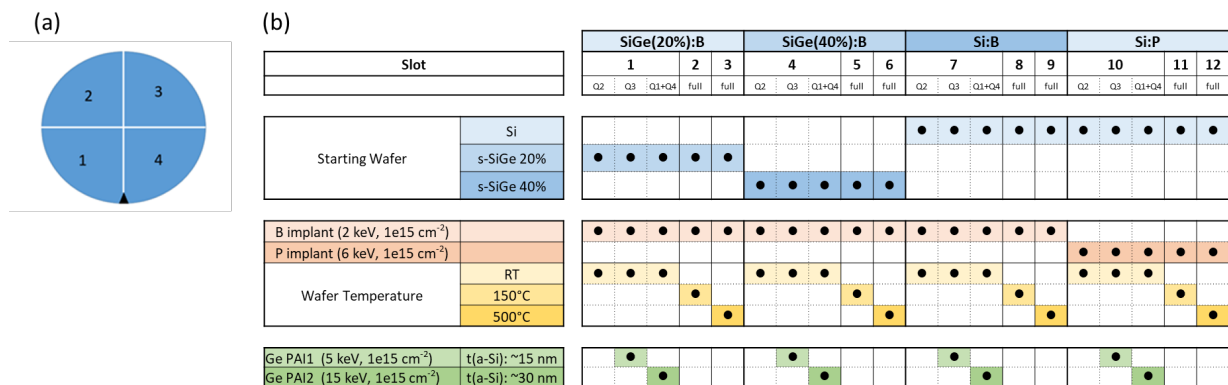|		SiGe(20%):B					SiGe(40%):B					Si:B					Si:P				
Slot		1			2	3	4			5	6	7			8	9	10			11	12
		Q2	Q3	Q1+Q4	full	full	Q2	Q3	Q1+Q4	full	full	Q2	Q3	Q1+Q4	full	full	Q2	Q3	Q1+Q4	full	full
Starting Wafer	Si											●	●	●	●	●	●	●	●	●	●
	s-SiGe 20%	●	●	●	●	●															
	s-SiGe 40%						●	●	●	●	●										
B implant (2 keV, 1e15 cm⁻²)		●	●	●	●	●	●	●	●	●	●	●	●	●	●	●					
P implant (6 keV, 1e15 cm⁻²)																	●	●	●	●	●
Wafer Temperature	RT	●	●	●			●	●	●			●	●	●			●	●	●		
	150°C				●					●					●					●	
	500°C					●					●					●					●
Ge PAI1 (5 keV, 1e15 cm⁻²) t(a-Si): ~15 nm			●					●					●					●			
Ge PAI2 (15 keV, 1e15 cm⁻²) t(a-Si): ~30 nm				●					●					●					●		

Figure 7: (a) Splitting of the wafer into 4 quadrants (Q1, Q2, Q3 and Q4) and (b) Details of thermal implant conditions in Si and SiGe samples for Tasks 2.1 and 2.2.

All the wafers were annealed using a ns laser in the submelt regime. First of all, the melt threshold (E_m) was determined from *in situ* Time-Resolved Reflectometry (TRR) maps in order to identify the process windows. Then, for each quadrant, small areas were processed with different energy densities (ED) and number of pulses using ns laser annealing in the sub-melt regime:

- Non-amorphized samples: E_m-5%, E_m-10%, E_m-15% and E_m-20% with 1, 10, 100 or 1000 pulses
- Amorphized samples: E_m-2.5%, E_m-5%, E_m-7.5% and E_m-10% with 1, 10, 100 or 1000 pulses

This is illustrated in Figure 8 and the different laser annealing conditions used for each quadrant are summarized in Figure 9.
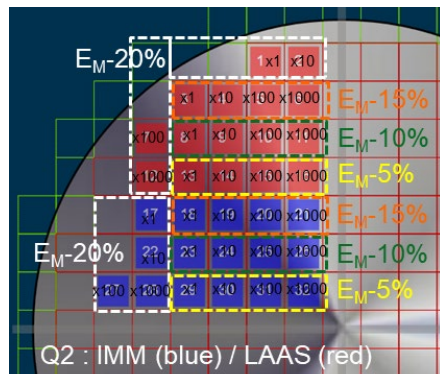
Figure 8: Example of ns laser annealing conditions employed for a quadrant. The conditions were repeated twice (red and blue areas).

	Slot	#01-Q1	#01-Q2	#01-Q3	#02-Q2	#03-Q2	#04-Q1	#04-Q2	#04-Q3	#05-Q2	#06-Q2	#07-Q1	#07-Q2	#07-Q3	#08-Q2	#09-Q2	#10-Q1	#10-Q2	#10-Q3	#11-Q2	#12-Q2
E1	E_m-5% (-2.5%)	1.025	1.425	1.125	1.425	1.475	0.875	1.25	1.025	1.25	1.275	1.175	1.65	1.325	1.65	1.70	1.175	1.275	1.225	1.325	1.575
E2	E_m-10% (-5%)	1.000	1.35	1.1	1.35	1.40	0.850	1.20	1.000	1.20	1.225	1.15	1.55	1.275	1.55	1.60	1.15	1.25	1.20	1.275	1.500
E3	E_m-15% (-7.5%)	0.975	1.275	1.05	1.275	1.325	0.825	1.125	0.975	1.125	1.15	1.10	1.475	1.25	1.475	1.50	1.10	1.20	1.15	1.25	1.400
E4	E_m-20% (-10%)	0.950	1.20	1.025	1.20	1.25	0.800	1.05	0.950	1.05	1.075	1.075	1.375	1.225	1.375	1.425	1.075	1.175	1.125	1.225	1.325

Figure 9: Summary of the energy densities employed (in J/cm^2) for the different quadrants.

It should be pointed out that for P implants done at RT and 150°C (Q2 of wafer 10 and wafer 11, respectively), unexpected melt and explosive recrystallization were observed during laser annealing as shown in Figure 10. This is due to the fact that the dose and energy conditions employed for P-implants leads to a partial amorphization of the Si substrate (~15 nm). This behavior was not observed for 500°C implants.
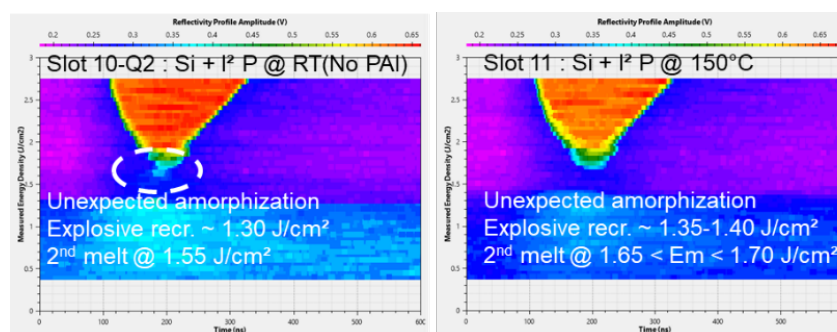

Figure 10: Cumulative TRR maps from 0.4 to 2.7 J/cm^2 (1 pulse, step 50 mJ/cm2) of P-implanted wafers at RT (left) and at 150°C (right) showing an unexpected explosive recrystallization.

2.2 Characterization

For all the samples, Haze analysis (optical measurement to evaluate the roughness of the surface) and sheet resistance measurements were systematically carried out at CEA-Leti. Therefore, for the different energy densities that have been used during laser annealing, the evolution of the Haze signal and the sheet resistance have been monitored as a function of the number of pulses.

The Spreading Resistance Profiling (SRP) technique is an established methodology that is in widespread use in both industry and research for measuring resistance profiles and, following calibration, the density profiles of active carriers in state-of-the-art semiconductor geometries. It is schematically exemplified in Figure 11 and explained in the following.
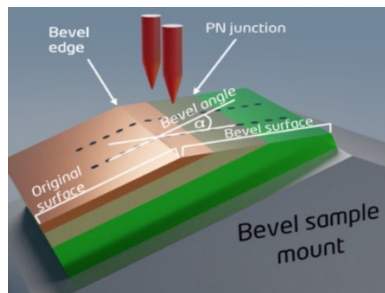
Figure 11: Schematic SRP measurement arrangement.

Two metallic probes, between which a small potential of 5 mV is applied, are used to quantify the charge carrier distributions as a function of depth. Depth information is obtained by stepping down the probes along a beveled surface of the sample. During the measurement a resistance profile is acquired, which is computed and converted into resistivity and carrier concentration by means of calibration curves, mobility parameters of monocrystalline Si and particular algorithms, which correct for sampling volume effects in case of ultra-shallow profiles [6]. Figure 12 shows the experimental calibration curves, needed to quantify the measured data. For that purpose, reference samples of the same crystallographic orientation and of known resistivity are accurately grinded using diamond and analyzed subsequently. A further step is done by means of the so-called Thurber plot, which accounts for the charge carrier mobility in monocrystalline Si. The final concentration distributions are then extrapolated after a multilayer analysis calculation, which corrects the resistivity for field effects from underlaying layers. SRP is characterized by an extremely wide dynamic range, covering about ten orders of magnitude, from near intrinsic material up to the solid solubility of the main dopant species in Silicon. By proper sample preparation, depth resolution down to 1 nm is achievable.
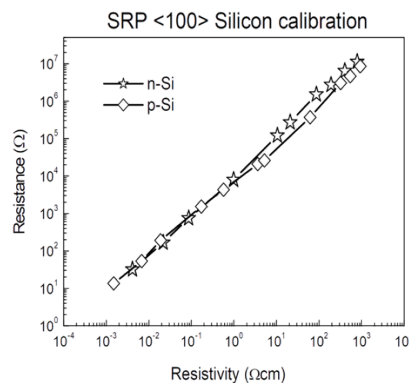

Figure 12: Experimental SRP calibration data for <100> n and p Si.

Considering the specific properties of the implanted region and of the activation processes investigated within the MUNDFAB project studies, a configuration of the apparatus suitable for ultra-shallow layers was chosen, in order to optimise both the measurement noise and the sensitivity of the technique. For that kind of equipment setup, the probes had to meet specific requirements, such as a low surface penetration and a non-rectifying behavior with proper I-V characteristics for structures with features of interest down to 100 nm or less in thickness. Furthermore, the analysis of the profiles could not be done without a special attention to the preparation of the samples. Damage to the silicon surface during diamond grinding had to be kept to a minimum and the bevel edge had to appear as a distinct sharp line. The main goal was to obtain a smooth surface finish, which assured low measurement noise and a well-defined bevel edge, so that the starting point of the profile could be accurately located. For this purpose, all samples were covered with a thin oxide layer, deposited by PECVD at very low temperature (~100°C). The final grinding procedure was then done by means of a very high quality, oil-based, diamond slurry, applied to a slow rotating frosted glass plate.

The doped layers analysed in this work by SRP required a particular correction procedure, which accounted for the so called "bevel edge effect", a severe artifact when dealing with ultra-shallow profiles. It has been demonstrated in the literature that, in this kind of structures, the measured resistance will start to increase monotonically when the tips are moved on the original sample surface, well before reaching the actual bevel edge [7]. This is due to the mechanical removal of silicon during the bevelling procedure and, if not accounted for, it results in a considerable underestimation of the active dose, because the measured raw data is too high. In order to achieve accurate carrier concentration distributions, in our laboratory we successfully have been using a very simple correction method for many years. It consists of calculating a damage related resistance and consequently correcting the measured profile. First of all, the additional resistance is defined as the difference between the spreading resistance measured on the top surface (far enough away from any borders and boundaries once the deposited oxide has been chemically etched), and the value found at the very first point of the profile on the beveled surface. This amount is then subtracted manually from the entire profile and only at that point, the resistance data are elaborated and converted in the final resistivity and carrier concentration profiles.

Also, Hall effect measurements were performed using a HL5500PC system from Accent with currents between 0.1-1.0 mA and a permanent magnetic field of 0.3 T. For reproducibility and reliability considerations, all electrical results presented below are obtained from multiple measurements on the same structure. These measurements were made using dedicated Van der Pauw structures shown in Figure 13. The fabrication process is divided in three main steps [8]. First, the design of the MESA structures (yellow), achieved by combining a positive resist development and a Reactive Ion Etching (RIE) process. Then, a negative resist is patterned to allow the deposition of aluminum (300nm) in the opened area corresponding to metallic contacts. The final step consists in annealing the final structures in order to enable the Al-Si interpenetration, considerably improving the contacts quality (ohmic contacts).
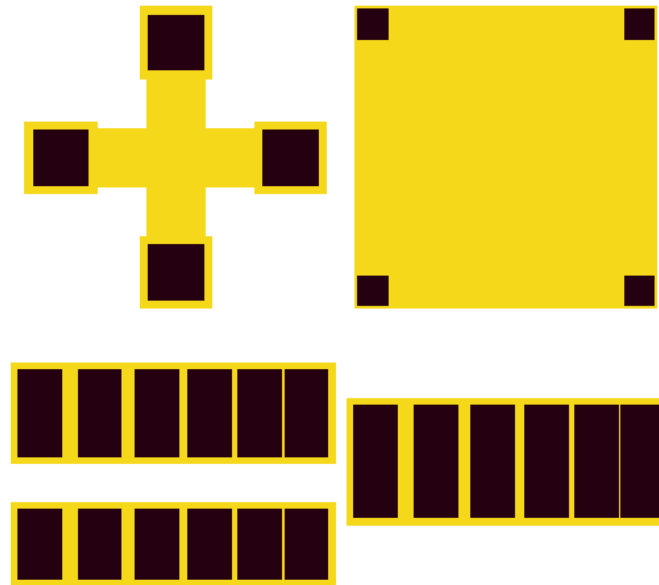
Figure 13: Layout used to fabricate cross and square-shaped Van der Pauw structures for hall measurements. Two levels of mask are showed: a level for the MESA structures (yellow) and another for metallic contacts (black). Transfer Length Measurements (TLM) structures were also processed in case contact optimisation was required.

2.3 General overview of experimental results

2.3.1 P-implanted samples

The evolution of Haze and Sheet Resistance (Rs) as a function of number of pulses for the 4 studied energy densities is shown in Figure 14. As discussed in Section 2.1, P implants done at RT and 150°C (wafers 10 and 11, respectively) partially amorphized the Si substrate. Therefore, the results shown in Figure 14.a and b should be interpreted carefully. A common trend is observed for the evolution of the sheet resistance values, with Rs always decreasing when increasing the number of laser pulses. Moreover, Rs is systematically lower for the EDs closest to the melt threshold, except for E1 of the RT-implanted sample (explosive recrystallization). A more detailed discussion about the structural and electrical behaviour of these wafers will be presented in section 2.5.
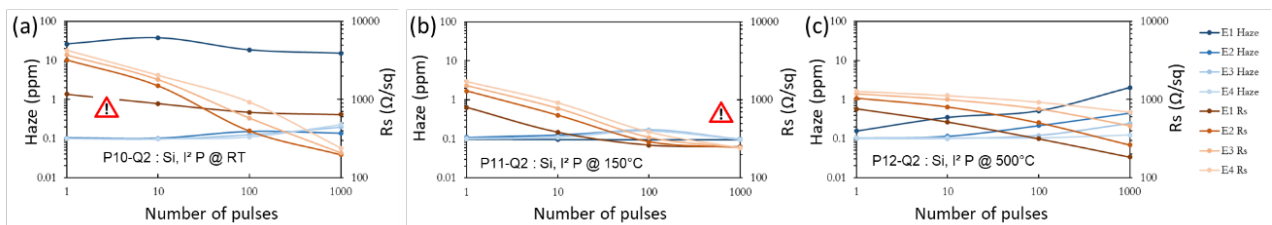

Figure 14: Haze and sheet resistance measurements as a function of number of pulses for (a) P10-Q2 (P implanted at RT) (b) P11-Q2 (P implanted at 150°C) and (c) P12-Q2 (P implanted at 500°C) Si samples.

2.3.2 B-implanted samples

The evolution of Haze and Rs as a function of number of pulses for the 4 studied energy densities is shown in Figure 15, Figure 16 and Figure 17 for SiGe 20%, SiGe 40% and Si

substrates, respectively. For the different cases, Rs always decreases with the number of pulses and the lowest value is systematically achieved for the energy density that is the closest to the melt threshold. Haze tends to increase with the number of pulses, especially for high ED values.
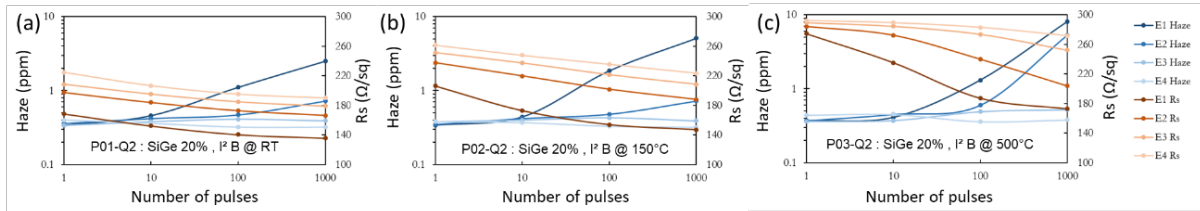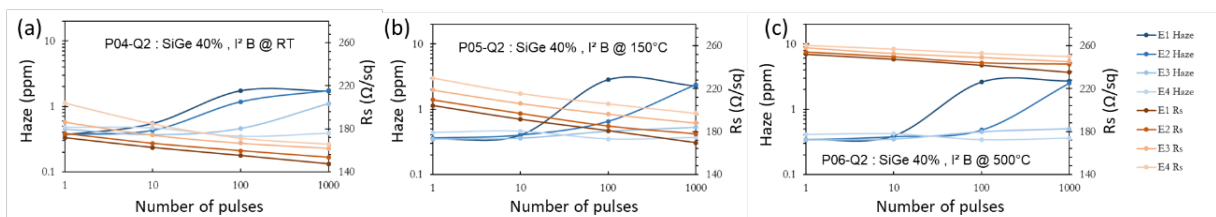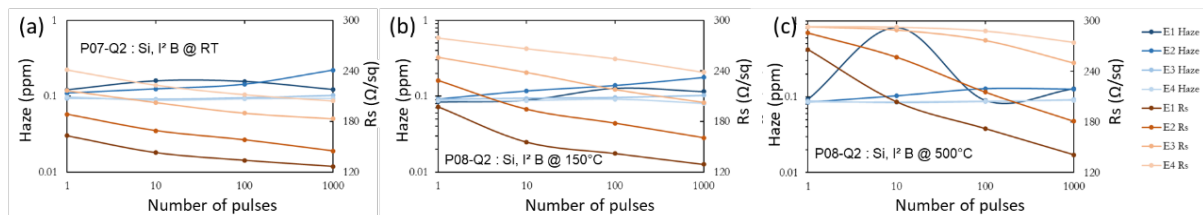

Figure 15: Haze and sheet resistance measurements as a function of number of pulses for (a) P01-Q2 (B implanted at RT) (b) P02-Q2 (B implanted at 150°C) and (c) P03-Q2 (B implanted at 500°C) SiGe 20% samples.

Figure 16: Haze and sheet resistance measurements as a function of number of pulses for (a) P04-Q2 (B implanted at RT) (b) P05-Q2 (B implanted at 150°C) and (c) P06-Q2 (B implanted at 500°C) SiGe 40% samples.

Figure 17: Haze and sheet resistance measurements as a function of number of pulses for (a) P07-Q2 (B implanted at RT) (b) P08-Q2 (B implanted at 150°C) and (c) P09-Q2 (B implanted at 500°C) Si samples.

2.4 Additional investigations of B-implanted Silicon samples

2.4.1 Spreading Resistance measurements

We applied the dedicated SRP methodology to study the multi-pulse laser annealing activation process in the sub-melting regime described previously for the cases of heated B implants. The cases which have been analyzed are summarized in Table 4.

Table 4: Samples analysed by SRP. The numbers refer to the identification of the samples in Figure 8.

Wf 08 Si:B – Implant temperature: 150°C

Pulses ED	x1	x10	x100	x1000
E1 (E_m – 5%)				32
E2 (E_m – 10%)				
E3 (E_m – 15%)				
E4 (E_m – 20%)	17			

Wf 09 Si:B B – Implant temperature: 500°C

Pulses ED	x1	x10	x100	x1000
E1 (E_m – 5%)	29	30	31	32
E2 (E_m – 10%)			25	
E3 (E_m – 15%)			20	
E4 (E_m – 20%)	17		27	

In Figure 18, the B active profiles measured after the irradiation at higher laser fluence (-5% with respect to the melting threshold) are shown for processes with 1, 10, 100, 1000 pulses for implanted B at 500°C substrate temperature at a dose of 1.0×10^{15} ions×cm^{-2}. The global activation shows a rapid increase in the 1-10 pulses range, reaching the 17% of the implanted dose, then a slower trend is visible in the 10-1000 pulses range, where it passes from 17% to 41% of the total dose. The space dependent activation seems to have two different mechanisms, namely in the surface region close to Rp (*i.e.* at a depth below ~80nm where a clear kink is visible in the active profiles) and in the deeper zone. Indeed, in the implant tails the activation saturates faster than close to the surface region. We notice that a high density of initial implanted defects are present in this latter region, while the implanted ions should reach the deeper zone by a channeling mechanism which could distribute the defects at a lower density in a broader space range. These different defect distributions could impact the local activation trend.
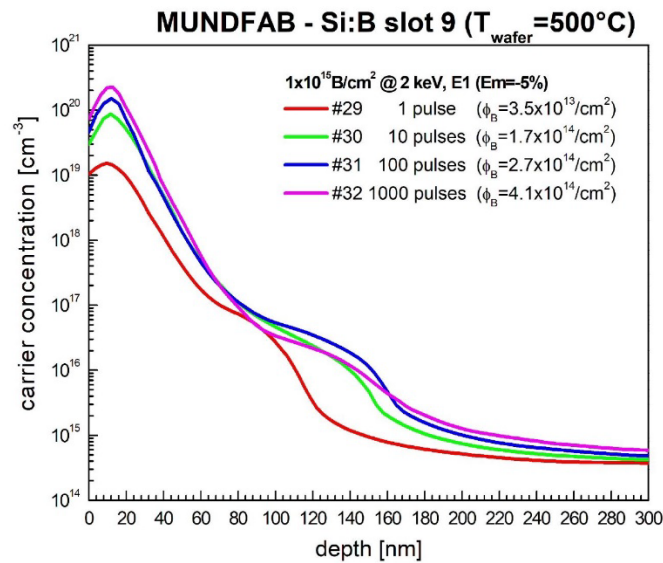
Figure 18: SRP B active profiles measured after the LA process irradiations at the highest laser fluence (-5% with respect to the melting threshold) after 1 (red line), 10 (green line), 100 (blue line), 1000 pulses (magenta line). The initial profile is a sample with B implanted (2keV energy) at 500°C substrate temperature to a dose of $1.0×10^{15}$ ions×cm^{-2}.

The dependency of the activation efficiency on the fluence for a fixed number of 100 pulses is shown in Figure 19. The rapidly varying thermal budget obtained for the -15% and -20% cases is too limited to permit an efficient activation and cumulated values, in spite the of relatively large number of pulses, are 0.3% and 1.4 %. A noteworthy improvement of the activation is obtained for larger fluences (-5% and -10%) and, therefore, this analysis allows an estimation of the convenient fluence process window for this multi-pulse process. From a close inspection of the profile, similar comments for the space dependent activation mechanism can be derived also for the varying fluence analysis: no significant variation of local activation efficiency in the profile tails is observed for the -5%, -10% (*i.e.* a saturation is achieved at these fluence level), whilst in general a faster local activation trend can be observed in the profile tails close to Rp region.
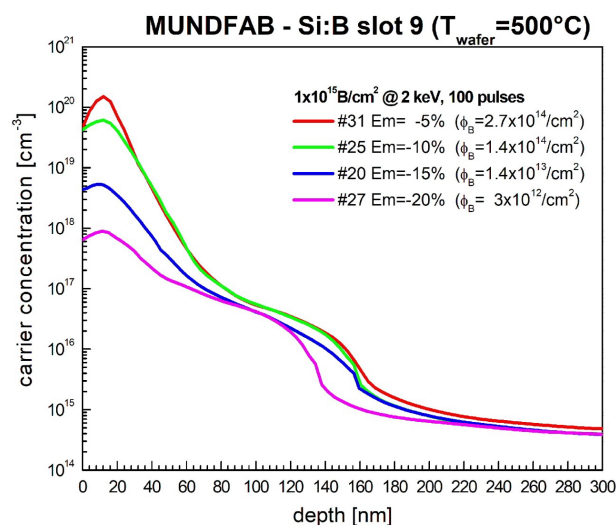

Figure 19: SRP B active profiles measured after the LA process irradiations for fixed number of pulses (100) for four different fluences (-5%, -10%, -15%, -25% with respect to the melting threshold). The initial profile is a B implanted (2keV energy) sample at 500°C substrate temperature to a dose of $1×10^{15}$ ions×cm^{-2}.

The role of the implantation temperature, which can have an impact on both the implanted chemical profile shape and the implantation defect distribution, is shown in Figure 20. The fact that the fluence case of -5 % belongs to the optimal process window is confirmed for both implantation temperatures, however for the 150°C case we can observe about one order of magnitude increase in the global activation efficiency with respect to the 500°C case (from 0.11% to 1.2% for the single impulse case) as shown in Fig.20. The double activation mechanism seems confirmed also for the lower temperature case but the tail effect seems less pronounced indicating a different initial distribution of the implanted B (e.g. a lower channeling effect).
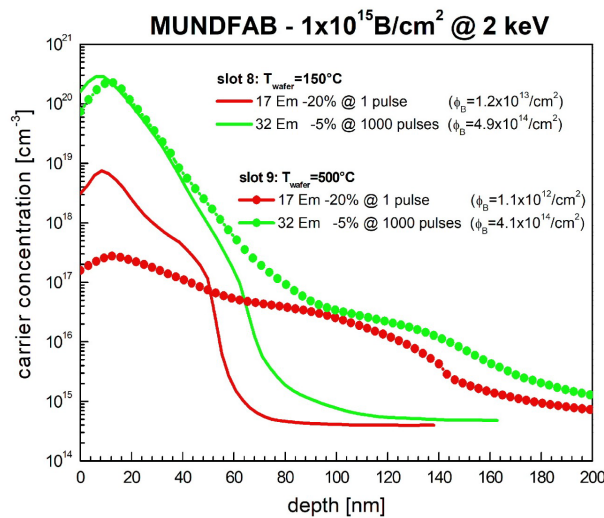

Figure 20: SRP B active profiles measured after the LA process irradiations for two choices of laser fluences and number of pulses: a) -5% with respect to the melting threshold and 1000 pulses (red lines); b) -20% with respect to the melting threshold and 1 pulse (green lines). In addition two different implantation temperatures are considered for the B (2keV energy) implanted profile (dose of 1.0×10^{15} ions×cm^{-2}): 150°C (solid lines) and 500°C (lines and dots).

All these finding need to be compared with chemical (SIMS) analysis of the implanted profiles after laser annealing (in progress) as well as with process simulations. A preliminary analysis of the comparison between SRP measurements and process simulations is reported in the next section. A complete discussion (including the missing SIMS profiles) will be reported during the forthcoming technical meetings as well as in the final consortium report.

2.4.2 KMC preliminary results on implanted B-profiles

A complete report on the simulations and the associated calibration will be given in Deliverable D2.6. Nevertheless, a few selected first results are shown here. The simulations have been carried out with Sentaurus Process from Synopsys with AdvancedCalibration [3], using a KMC solver, without any further calibration.

The simulation results of the profiles after boron implantations (2 keV, 1×10^{15} cm^{-2}) at 150 °C and 500 °C, are shown in Figure 21, together with measured profiles obtained by SIMS. Also

shown in the figure are the SRP profiles after 1 pulse of laser annealing with energies of E1 and E4 as given in Fig.9

First of all, the simulations predict significantly deeper B-profiles than can be observed in SIMS measurements. This is possibly due to the calibration of the SIMS, and new measurements are planned to overcome this issue. In the 500 °C-case, the simulations predict a relatively high activation in the tail region. One can speculate that the activation after the 1st pulse should be higher than the activation after implantation, however, the simulated as-implanted concentration profile of active B is higher than the carrier concentration obtained by the SRP measurement of the 1-pulse-E4 sample for the entire depth. The measured activation in the 1-pulse-E1 case is only higher than the simulated as-implanted profile in the first 50 nm.
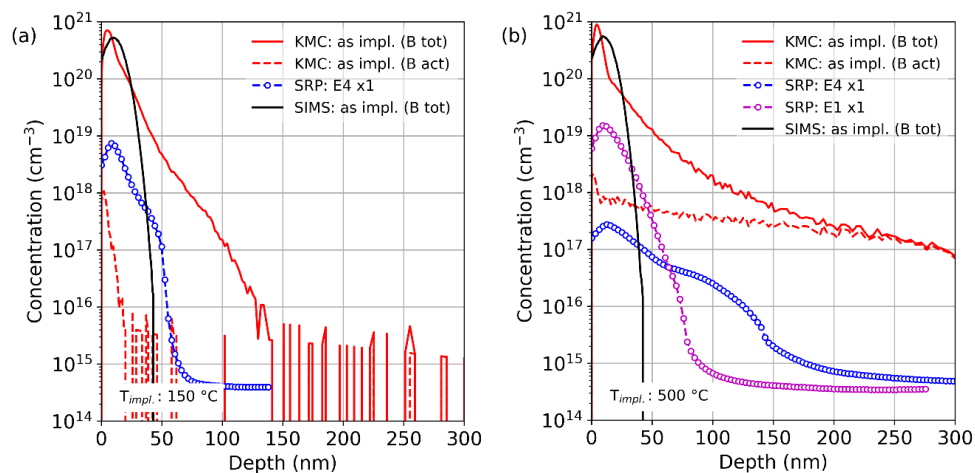

Figure 21: KMC Simulation results of as implanted B-profiles after implantation at (a) 150 °C and (b) 500 °C compared to measurements by SIMS and SRP. The profiles of active B in SRP measurements were measured after laser annealing 1 pulse and with fluences of (a) E4 and (b) E4 and E1 (and are compared to as-implanted active B of KMC simulations).

For the simulations of the laser annealing, temperature vs. time profiles of the pulses corresponding to the different fluences were provided by CNR from simulations of the laser annealing process. For the simulations here, it is assumed that the temperature is constant throughout the topmost silicon layer with the dopant profile. The profiles are shown in Figure 22.
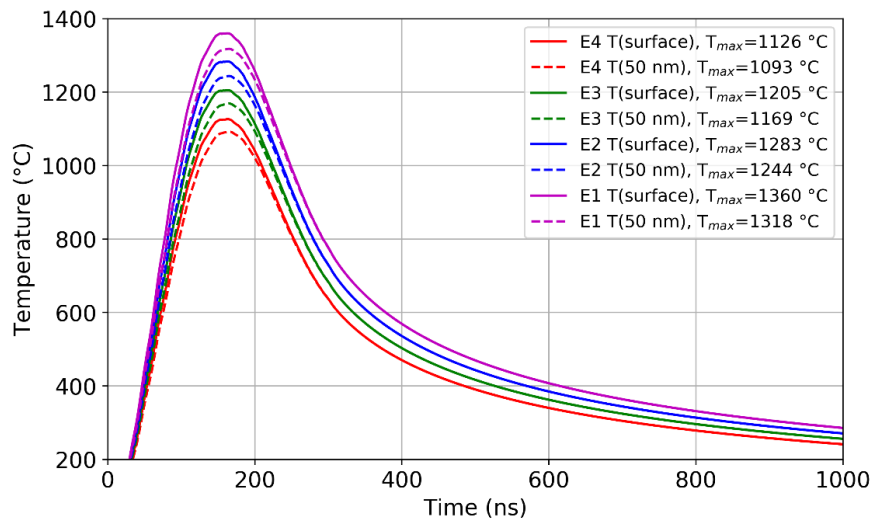
Figure 22: Temperature vs. Time of one pulse for the different fluences. The temperatures at the surface are plotted in solid lines and the temperatures 50 nm below the surface are plotted with dashed lines.

The simulation results of the active B concentration compared to the profiles obtained from SRP measurements after 1-1000 pulses with E1 fluence are shown in Figure 23.a. The samples were all implanted at 500 °C. The profiles obtained from simulation have more shallow peaks of active B, and longer tails. Still, the trends of the simulation results and the SRP measurements are similar in the sense that the active B concentration at the surface increases with the number of pulses at a comparable rate. This trend is summarized in Figure 23.b where the maximum active concentration is plotted against the number of pulses.
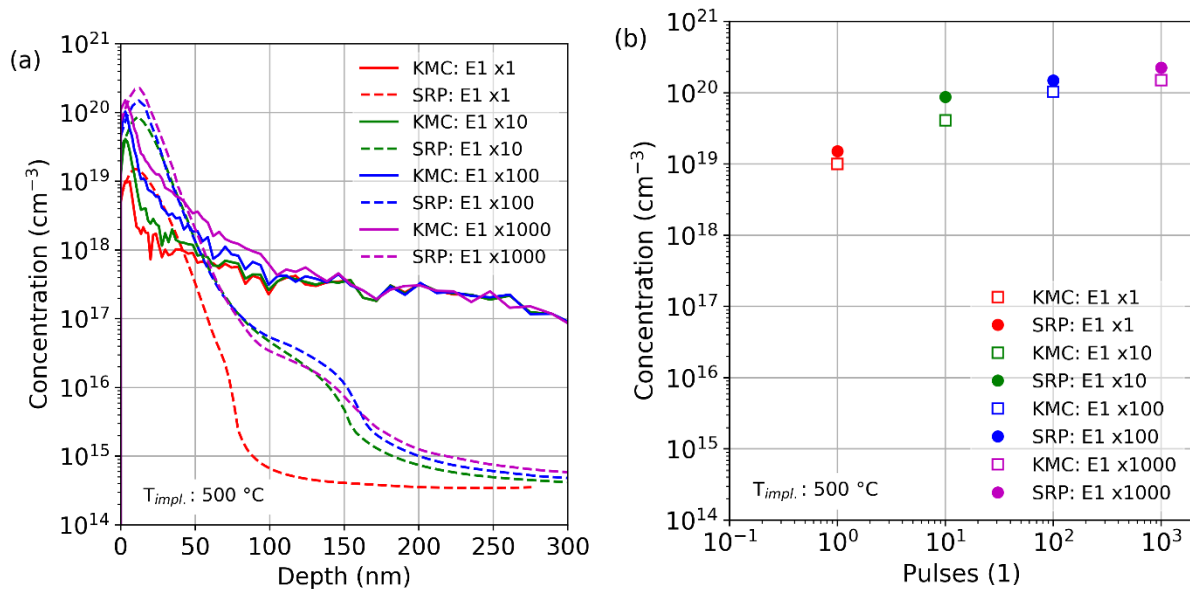

Figure 23: (a) Simulation results (KMC) of the active B concentration (solid lines) compared to the profiles obtained from SRP (dashed lines) after 1-1000 pulses (fluence = E1). (b) Peak concentration of the active B concentration of the simulation results (squares) and profiles obtained from SRP measurements (circles).
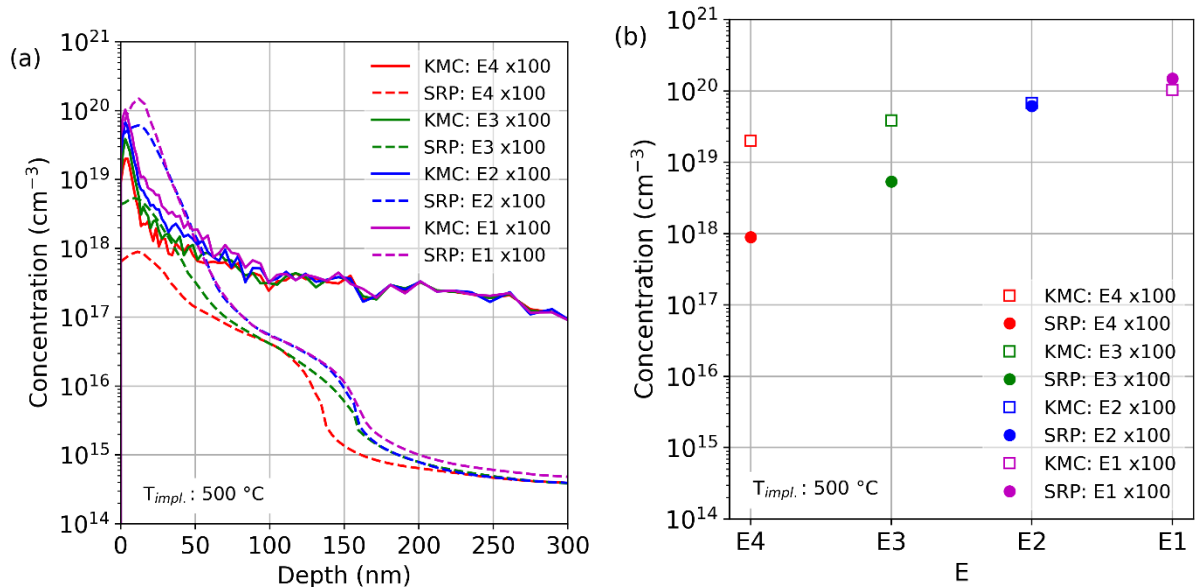
Figure 24: (a) Simulation results (KMC) of the active B concentration (solid lines) compared to the profiles obtained by SRP (dashed lines) after 100 pulses at different fluences (E1-E4). (b) Peak concentration of the active B concentration of the simulation results (squares) and of the SRP profiles (circles).

The simulation results of the active B concentration compared to the profiles obtained from SRP measurements after 100 pulses with different fluences, E1-E4, are shown in Figure 24.a. The samples were all implanted at 500 °C. The peaks in the active B concentration of the simulations are, for all fluences, shallower than in the measurements. There is a larger difference due to the fluence in the profiles obtained from the SRP measurements compared to the ones from the simulations. The simulation results predict a much higher activation for the two lower fluences, E3 and E4. This trend is summarized in Figure 24.b, which shows the maximum values of the active B concentration vs. fluence for the simulations and the measurements.

In Figure 25, the SRP measurements of the two extreme cases are shown, 1-pulse-E4 and 1000-pulses-E1. These cases correspond to the annealings with the smallest and largest thermal budget, respectively. The measured data is compared to the simulation results, showing the active and total B concentration. In Figure 25.a, the B was implanted at 150 °C, and in Figure 25.b, at 500 °C. These results highlight that the simulations overestimate the activation after 1 pulse with the E4-fluence, and that the simulations underestimate the activation after 1000 pulses with the E1-fluence. This is probably due to the initial activation overestimated by the simulation of the heated implantation.
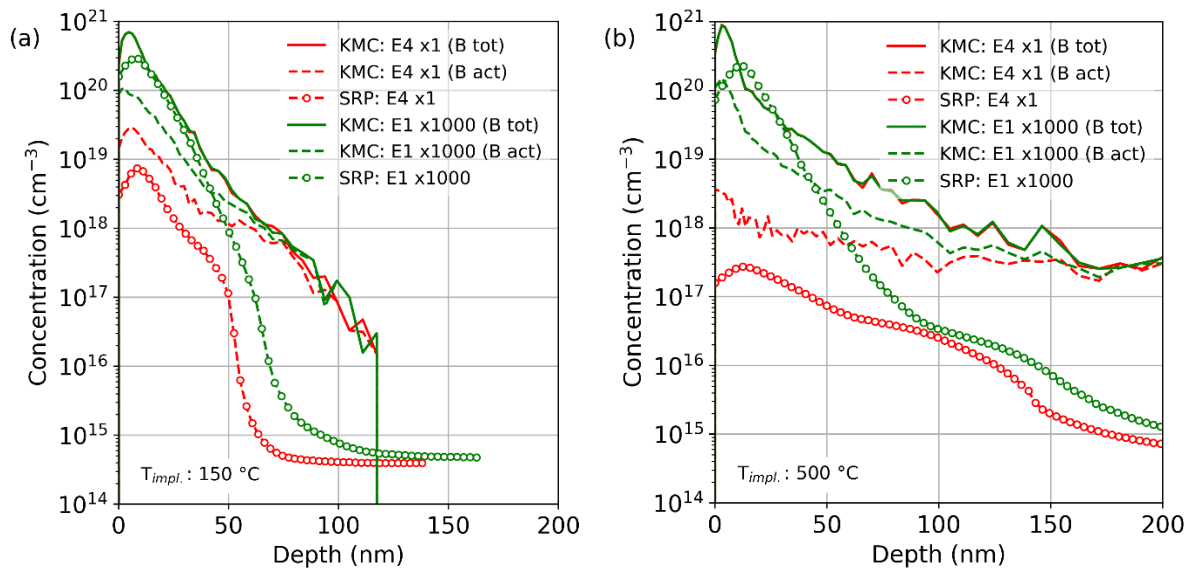
Figure 25: Simulation results (KMC) of the B concentration, total and active compared to the profiles obtained by SRP for two cases: after 1 pulse with the E4-fluence and after 1000 pulses with the E1-fluence, for wafers implanted at (a) 150 °C and (b) 500 °C.

Finally, this comparison of the carrier concentration profiles obtained from the SRP measurements and simulations using Sentaurus Process of Synopsis with AdvancedCalibration [5] suggests that a model evaluation and calibration related both to the heated implantation and to the activation through laser annealing is needed.

From the active boron profiles it is possible to calculate the sheet resistance of the different samples. The mobility is itself a function of the concentration of active boron and has been calculated using the analytical formula of [9]. The samples consist of an implantation of boron on a wafer which is itself lightly doped with boron, so there is no p-n junction in the samples. An accurate calculation of the sheet resistance should therefore in this case take into account the boron doping on the entire thickness of the wafer. However, it is possible to qualitatively compare the trends obtained in the sheet resistance values extracted from the simulations with the measurements performed in section 2.3.2 (cf. Fig. 17).
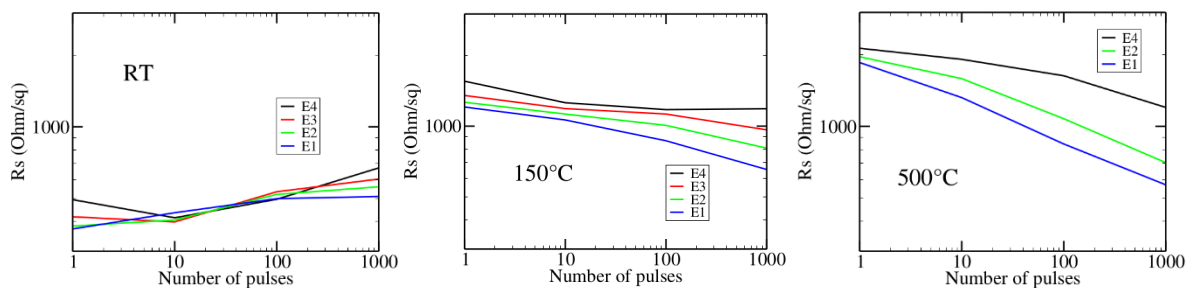

Figure 26 : Sheet resistances calculated from KMC predicted active boron profiles for implantation at RT (left), 150°C (middle) and 500°C (right) and for different laser fluence used and different pulses numbers.

Some trends are correctly simulated by the KMC. The relative order of sheet resistance as a function of implantation temperature for a low number of pulses is consistent between the predictions of the simulations and the measurements. The higher the implantation temperature, the higher the sheet resistance for a low number of pulses in both the simulations and the measurements (Figures 26 and 17). Another trend observed in both simulations and measurements is the evolution of the sheet resistance as a function of the laser fluence used

for implantation at 500°C. For this implantation temperature, the use of a higher laser fluence allows to activate more boron and thus to decrease the sheet resistance to a lower level for the same number of pulses.

However, the simulation fails to predict some experimental observations. For the samples implanted at RT the sheet measurements show a decrease in sheet resistance while an increase is predicted in the KMC simulations.

In order to understand the effect of implantation temperature and laser fluence, different simulated boron-interstitial clusters (BICs) kinds have been investigated. The different kinds of BICs can be described by the number of boron atoms n and the number of interstitials m in the cluster (which can be written as follows: $B_n I_{m)}$. In the histograms shown in Figure 27 it is observed that as the implantation temperature increases, more BICs with a large number of borons (n>5) and a moderate-low number of interstitials (m<7) are simulated after 1 pulse. These BICs with a large number of boron atoms are assumed to be more stable in the literature [10]. The heating of the wafer during implantation promotes the evolution of BICs towards these stable forms. These BICs contain more boron and therefore there is less active boron in the heated implantations.
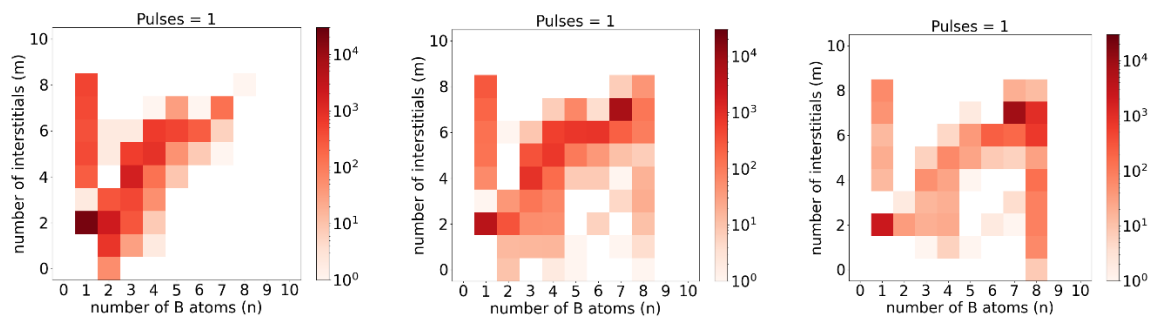

Figure 27 : Histogram of predicted BICs in KMC as a function of the number of boron atoms (n) and interstitials (m) in the cluster. From left to right are the histograms for the single-pulse annealed samples at E1 for RT, 150°C and 500°C implantation temperatures. The color bar represents the number of BICs of each type in the simulation box.

The difference in activation as a function of laser fluence after implantation at 500°C can be explained using the type of BICs formed. As mentioned, the BICs simulated at 500°C are more stable. The temperature required to dissociate these BICs is therefore higher. By using a laser fluence close to the fluence melting point it is possible to dissolve these BICs. This is less the case when using a lower laser fluence. In Figure 28 it is shown that after 1000 pulses using E4 fluence a large number of BICs with a large number of boron (n>6) remain. The laser annealing with E1 fluence manages to dissolve this type of BICs. These simulations are in agreement with results in literature [10].
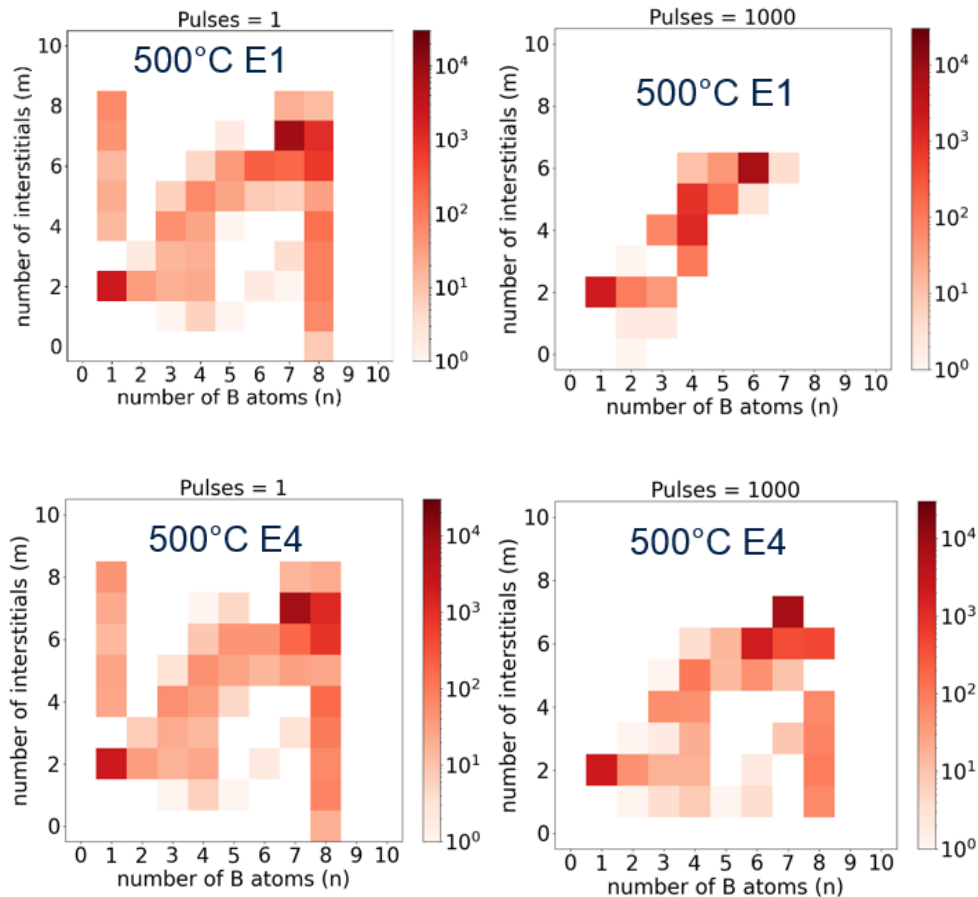
Figure 28 : Comparisons of the effect of 1000 pulses on the BIC histogram for samples implanted at 500°C and for fluences of E1 or E4 used for laser annealing.

2.5 Additional investigations of P-implanted Silicon samples

The surface reflectivity as a function of the number of cumulated laser pulses for the Si substrates implanted with phosphorus at different temperatures is reported in Figure 29. Four different laser energy densities (E1 to E4, cf. Figure 9) were investigated. For each annealed sample, the reflectivity at "zero" laser pulses corresponds to the one measured on the as-implanted sample. The highest values recorded at "zero" pulses come from wafer S10 implanted at RT and indicate, as expected, that this wafer was amorphised, in agreement with the implant conditions. In contrast, the low reflectivity values recorded from the wafer implanted at 500°C (S12) correspond to those of a crystalline surface, indicating that the residual damage contained in this wafer is extremely low. Finally, an intermediate value is measured in samples implanted at 150°C, possibly corresponding to a partial amorphisation of the implanted wafer.

Concerning wafer S10 (implanted at RT), the surface reflectivity decreases progressively down to the fully crystalline value (around 22%) for all laser energy densities, excepted for the highest one (E1). Such progressive decrease indicates that the initial amorphous layer is recrystallized by SPER, which is consistent with the observed evolution of both sheet resistance and haze values (cf. Figure 30a). In particular, for E2, E3 and E4, the sheet resistance decreases from around 3000 Ω/sq to 200 Ω/sq. Moreover, the surface morphology remains flat for all number of pulses conditions (cf Fig. 30b).

In contrast, for the highest laser energy density E1, the reflectivity initially exhibits a fast decrease following a single pulse anneal (associated to an explosive recrystallization (ER)

mechanism, cf. Figure 10a), then it stays constant at a higher value compared to single crystal silicon. This is probably due the explosive crystallization leading to the formation of a non-reversible polycrystalline Si layer. Indeed, following a significant improvement of R_S at 1 pulse and the corresponding increase of the haze signal [11] (cf. Figure 30a), both values remain stable up to 1000 pulses.
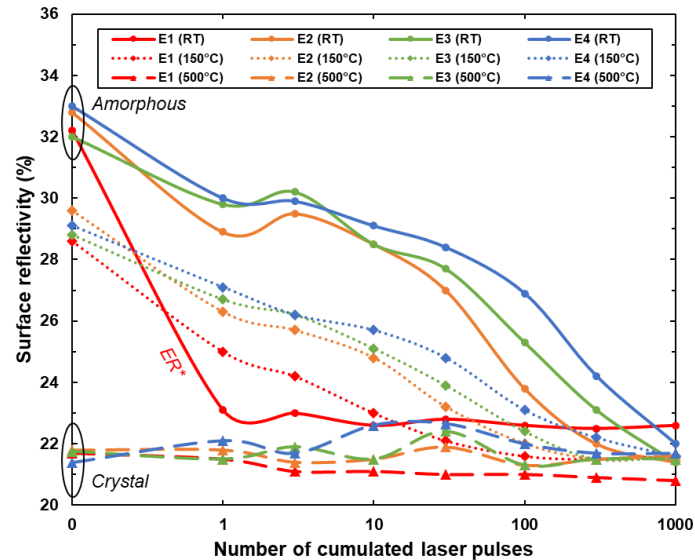

Figure 29: Surface reflectivity as function of the number of cumulated laser pulses for a Si substrate implanted with phosphorus at room temperature (RT) (straight lines), 150°C (dotted lines) and 500°C (dashed lines) at four different energy densities below the melt threshold. Layers implanted at RT and 500°C exhibits a surface reflectivity characteristic of amorphous and crystal layers. The abrupt change of surface reflectivity at (E1, RT, 1 pulse) corresponds to an explosive recrystallization (ER) phenomenon.

In the following, we present the conclusions based on the measurements made on Si wafers S11 and S12, corresponding to phosphorus-implanted Si at 150°C and 500°C, respectively (cf. Figure 7b). Hall measurements have been performed only on these two wafers, while work on wafer S10 is still in progress. Indeed, this wafer required a particularly careful preparation as it gathers 3 initial conditions divided in three areas: standard room temperature implantation (quarter 1) and two Ge pre-amorphization implantations (PAI) (quarter 2 and bottom half). Also, concerning the nanosecond laser annealing (NLA) conditions performed on the room temperature implanted-area, additional investigations and supplementary laser anneals were performed at CEA-LETI before cutting and shipping the wafer part to LAAS-CNRS. Consequently, the shipment of S10 to LAAS was delayed compared to wafers S11 and S12.
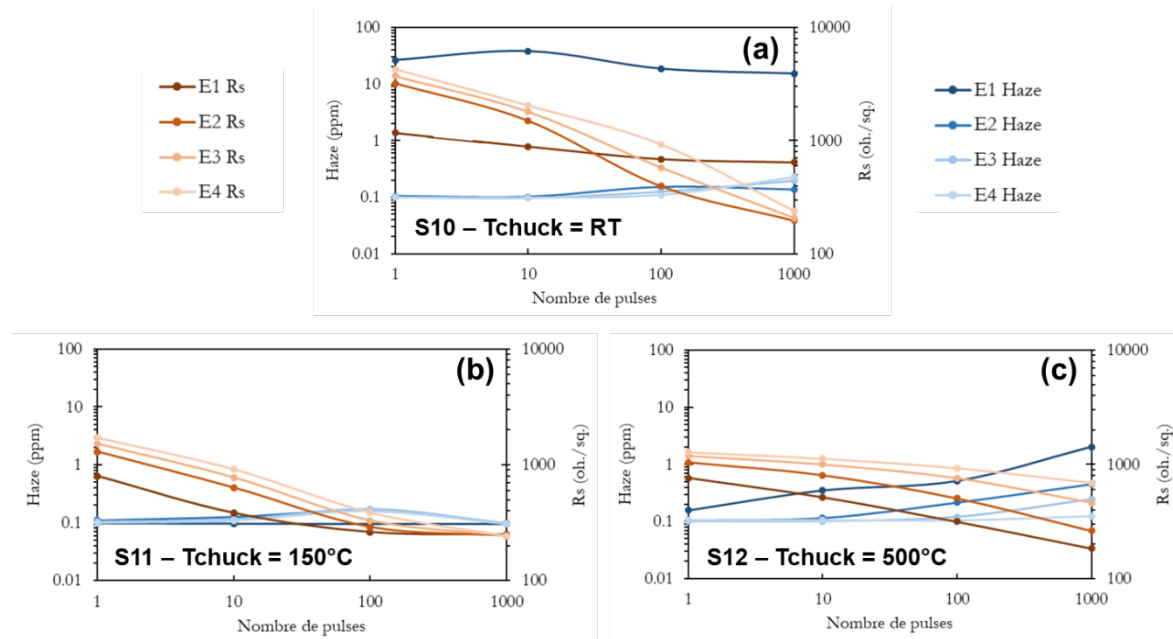
Figure 30: Sheet resistance (4PP) and haze measurements as function of the number of pulses for a Si substrate implanted with phosphorus at room temperature (RT) (a), 150°C (b) and 500°C (c) at four different energy densities below the melt threshold.

NLA was performed on wafers S11 and S12 using the conditions described in Figure 9. Four different energy density (ED) values below the melt threshold E_M were selected: $E_M - 5\%$ (E_1), $E_M - 10\%$ (E_2), $E_M - 15\%$ (E_3) and $E_M - 20\%$ (E_4). For these four ED conditions, several numbers of cumulative pulses were used: 1, 10, 100 and 1000 pulses, which gives a total of 16 conditions per wafer. The analysis of the electrical properties was conducted by gathering the results from Hall effect measurements with haze and Time-Resolved Reflectivity (TRR) analysis.

For S11 (150°C), the sheet resistance measurements made by 4PP at LETI and by the Van der Pauw method at LAAS are in very good agreement (Figure 31(a)), displaying a clear improvement of the conduction properties when increasing the number of pulses, for both studied energy densities E_1 and E_4. Similarly, Hall measurements have revealed an increase of the active dose going from 1 to 1000 pulses (Figure 31(b)). Considering the nominal implanted dose of 1.0x10^15 cm^-2, and taking a typical scattering factor r_H=1 for negative carriers, cumulative pulses improved the activation rate from 14% to 46% for E_1 and from 4% to 56% for E_4. When looking at the whole set of sheet resistance measurements for this wafer (cf. Figure 30b), it seems that a saturation regime is reached at 1000 pulses. This suggests that more cumulated pulses will not improve the activation rate further than 60% if the chosen energy density is kept below the melt threshold. In addition, Haze measurements presented in Figure 30b show a low surface roughness (around 0.1 ppm), even for a high number of pulses.

As discussed above, the initial "zero-pulses" surface reflectivity value for wafer S11 (150°C, cf. Figure 29) is intermediate between wafer S10 (RT), fully amorphized in the implanted region, and the wafer S12 (500°C), which has no amorphous phase. For this reason, it remains uncertain whether the thermal activation process of wafer S11 is a "standard" one (i.e. related to point defect recombination) or a SPER annealing process (Solid Phase Epitaxy Regrowth). TEM cross-section of the as-implanted layer will be conducted in the future to remove any uncertainty.
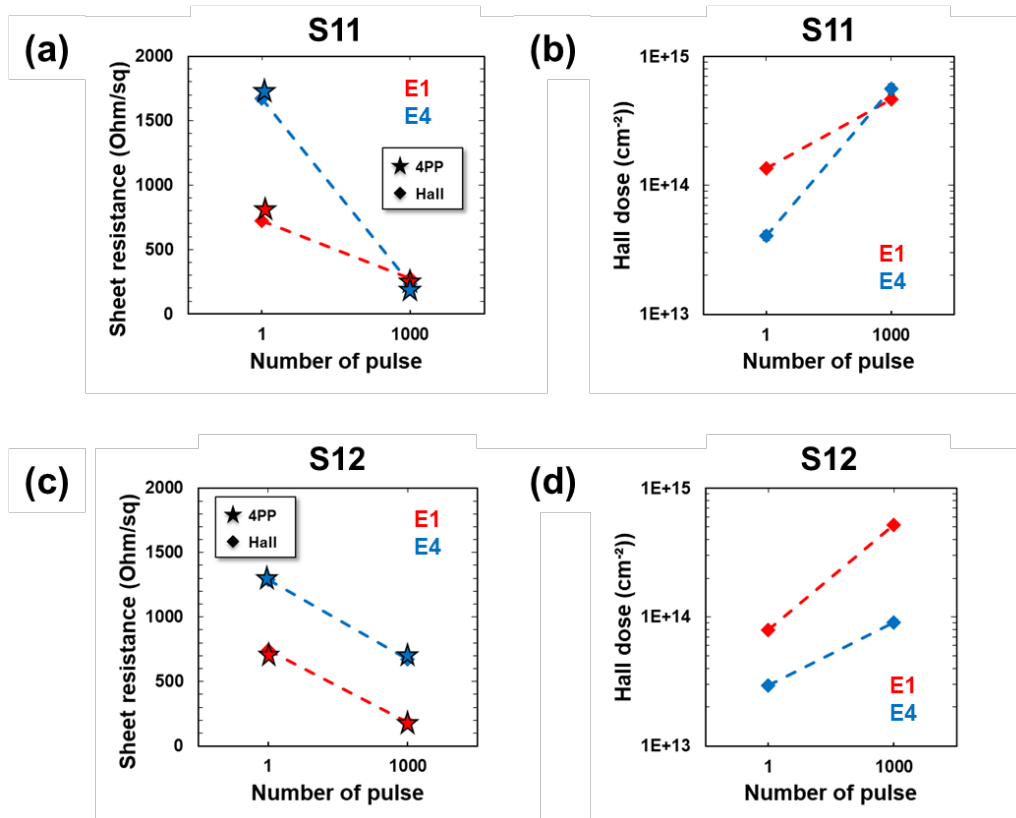
Figure 31: Electrical measurements made by LETI (4PP) and LAAS (Hall effect) on laser-annealed Si substrates implanted with phosphorus at 150°C and 500°C, corresponding to S11 and S12, respectively. Sheet resistance (a,c) and Hall dose (b,d) measurements as function of the number of pulse for energy densities E_1 and E_4, equivalent to conditions 5% and 20% below the energy density melt threshold E_M.

Finally, for wafer S12 (500°C), the sheet resistance improves when increasing the number of pulses (Figure 31c). The main difference with S11 is in the energy density E4 that does not allow an equivalent improvement of the conduction properties at 1000 pulses. This can also be seen in Figure 31(d), where the Hall active dose is improved but the maximum reached value is affected by the initial fixed energy density. The closer to the melt threshold the ED is chosen, the higher the reachable active dose will be. From 1 to 1000 pulses, E1 allows to climb from 8% to 52% while E4 gives an increase from 3% to only 9%. We suspect that the used chuck temperature during the phosphorus implantation might lead to the formation of a damaged, but still crystalline layer, i.e. containing stabilized clusters, which cannot be fully dissolved by applying laser annealing. To confirm this hypothesis, or at least investigate in-depth this phenomenon, TEM plane views will be performed on the four measured samples (E1 and E4 at 1 and 1000 pulses).

In terms of surface roughness, the haze values increase with the number of pulses from around 0.1 ppm to values between 0.1 ppm (E4) and 2 ppm (E1) ((c)). Thereby, a significant increase of the active dose is inevitably accompanied by a deterioration of the surface morphology.

In summary, despite the missing Hall data for wafer S10 implanted at RT, all the investigations carried out so far suggest that laser-induced SPER in the fully amorphised wafer S10 produces the best results among the three studied implantation conditions, both in terms of electrical properties and surface morphology.

2.6 Pre-amorphised structures – B-implanted samples

2.6.1 SiGe substrates

The evolution of the surface reflectivity in amorphized (at either 30 nm or 15 nm depth) B-implanted SiGe 20% and SiGe 40% samples is shown in Figure 32 and Figure 33, respectively. Explosive crystallization is detected at first pulse for 30 nm and likely for 15 nm for the highest ED value (E1). Figure 32 plots the final reflectivity of the samples after each laser pulse for various samples where 'final' means after complete cooling of the sample (not during the laser pulse). The explosive recrystallization (ER) detected for some samples, i.e. the ones amorphized over 15 & 30nm and submitted to the highest selected energy density, E1, is rather evidenced by the TRR data during the laser pulse. Indeed, during the laser pulse, if ER occurs, we can detect a sudden drop of the surface reflectivity due to the transition from liquid to solid (see the 3 graphs below). Without ER, the TRR signal decays regularly (graph on the left). With ER (graph in the middle is a typical obvious case), the TRR signal drops within < 5ns before the end of the laser pulse. Thus, the ER detection is rather based on real-time reflectivity drop detected during the laser treatment, rather than after each pulse. Figure 32 does not evidence such ER phenomenon directly. Nevertheless, we have some slight indications for the 15nm-amorphized sample: the final surface reflectivity (red data points) remains, after 1000 pulses at E1, slightly higher than the one after 1000 pulses at E2 or E3 (orange or green points). With E2 and E3, we are confident that the whole initially amorphized layer is now monocrystalline (minimum of reflectivity) while the surface reflectivity remains higher after ER (nanograins). For the sample amorphized over 30nm, only the real-time TRR curve (not shown in the deliverable, graph below in the middle) would prove the ER. In this case, Figure 32 does not provide any direct indication (partial SPER even for the other ED conditions). If we could further continue SPER with the lower ED values, we would expect the red curve remain higher than the 3 others (saturation for the red curve, not for the others).

For the 15 nm amorphized substrates, the reflectivity tends towards 23-24%, therefore a full recrystallization of the amorphous layer may have been completed. In contrast, for the 30 nm amorphized substrates, the reflectivity saturates at an intermediate level, probably indicating a partial SPER (~ 15nm). After recrystallization of a few nm, ED should therefore be increased to allow further SPER.
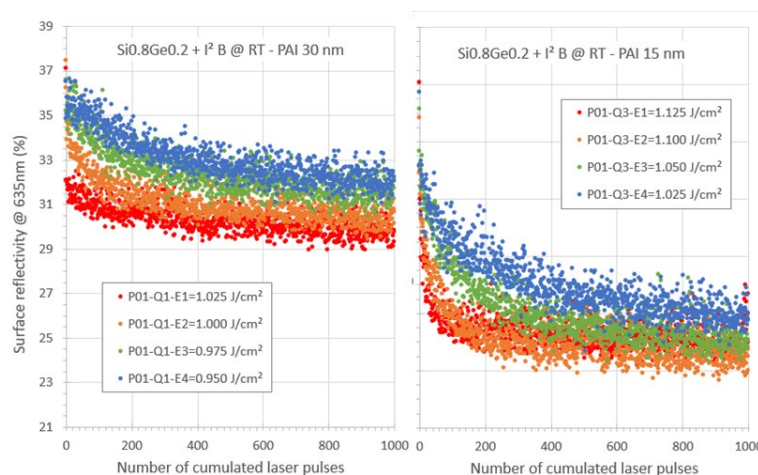

Figure 32: Evolution of the surface reflectivity (from TRR) as a function of the number of pulses in SiGe 20% samples for a 30 nm (left) and 15 nm (right) PAI.
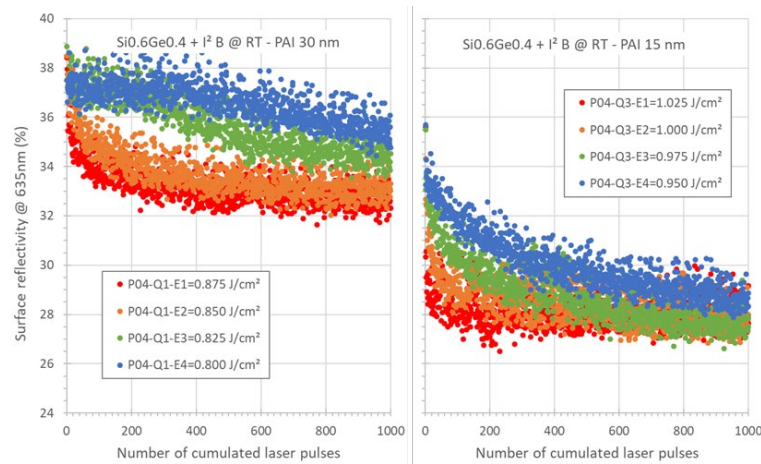
Figure 33: Evolution of the surface reflectivity (from TRR) as a function of the number of pulses in SiGe 40% samples for a 30 nm (left) and 15 nm (right) PAI.

The evolution of Haze and Rs as a function of number of pulses for the 4 studied energy densities is shown in Figure 34 and Figure 35 for SiGe 20% and SiGe 40% wafers, respectively. For 30 nm PAI, Rs remains high due to the partial SPER. For 15 nm PAI, the sheet resistance reaches equivalent values to other implant conditions. In case of ER (observed for E1), cumulative laser pulses may induce larger grains and/or SPER from the bottom if ER did not reach a/c interface.
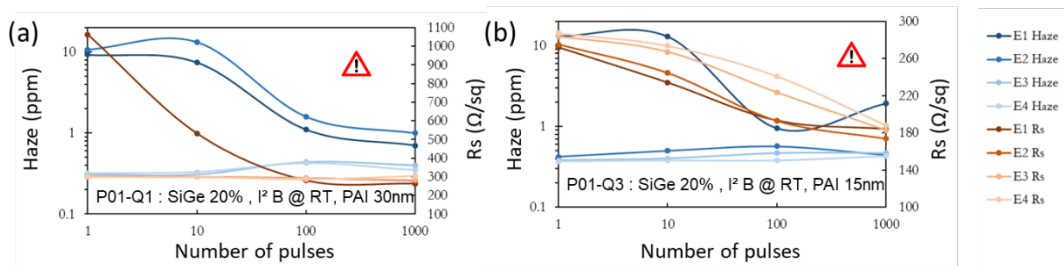

Figure 34: Haze and sheet resistance measurements as a function of number of pulses for (a) P01-Q1 (PAI 30 nm) and (b) P01-Q3 (PAI 15 nm) SiGe 20% samples
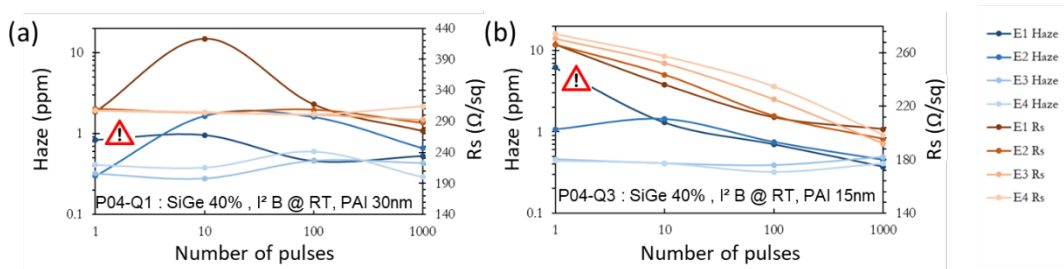

Figure 35: Haze and sheet resistance measurements as a function of number of pulses for (a) P04-Q1 (PAI 30 nm) and (b) P04-Q3 (PAI 15 nm) SiGe 40% samples

2.6.2 SiGe substrates

The evolution of the surface reflectivity in amorphized B-implanted Si samples is shown in Figure 36. Similarly, to SiGe samples, for PAI 15 nm, full SPER is probably achieved for E2-E4 energy densities. For PAI 30 nm, only partial SPER is observed for E2-E4 energy densities. For both PAI, E1 leads to an explosive recrystallization.
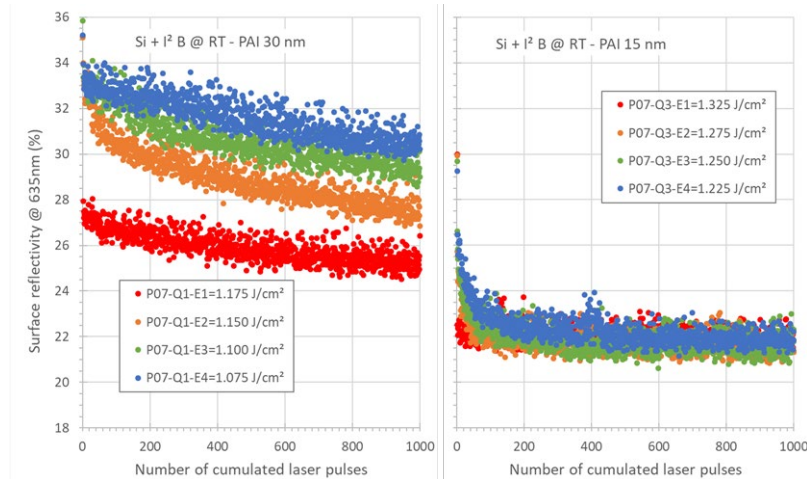

Figure 36: Evolution of the surface reflectivity (from TRR) as a function of the number of pulses in Si samples for a 30 nm (left) and 15 nm (right) PAI.

The evolution of Haze and Rs as a function of number of pulses for the 4 studied energy densities is shown in Figure 37. For the PAI 30 nm, Rs remains high due to the partial SPER while Haze does not show a clear trend. For PAI 15 nm, after 1000 pulses Rs reaches almost equivalent values to other implant conditions (except for E1 which leads to ER).
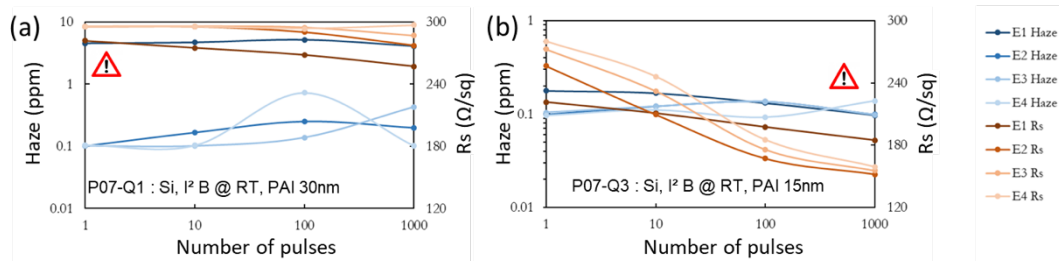

Figure 37: Haze and sheet resistance measurements as a function of number of pulses for (a) P07-Q1 (PAI 30 nm) and (b) P07-Q3 (PAI 15 nm) Si samples

2.7 Pre-amorphised structures – P-implanted samples

The evolution of the surface reflectivity as a function of number of pulses for the 4 studied energy densities is shown in Figure 38. As for B-implanted samples (SiGe or pure Si), the TRR measurement results suggest that a full SPER has been completed in 15 nm PAI samples while only partial SPER was achieved in 30 nm PAI samples, for E2-E4 energy densities. In both cases, E1 leads to an explosive recrystallization.
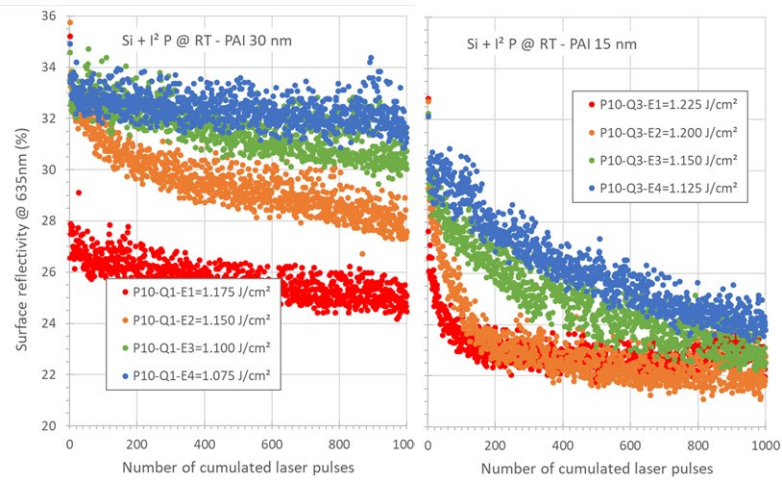
Figure 38: Evolution of the surface reflectivity (from TRR) as a function of the number of pulses in Si samples for a 30 nm (left) and 15 nm (right) PAI.

The evolution of Haze and Rs as a function of number of pulses for the 4 studied energy densities is shown in Figure 39. Similar conclusions can be drawn as for B-implanted samples. In PAI 30 nm samples, Rs remains high due to the partial SPER for E2-E4 energy densities. In PAI 15 nm samples, Rs reaches similar values as other implant conditions after 1000 pulses.
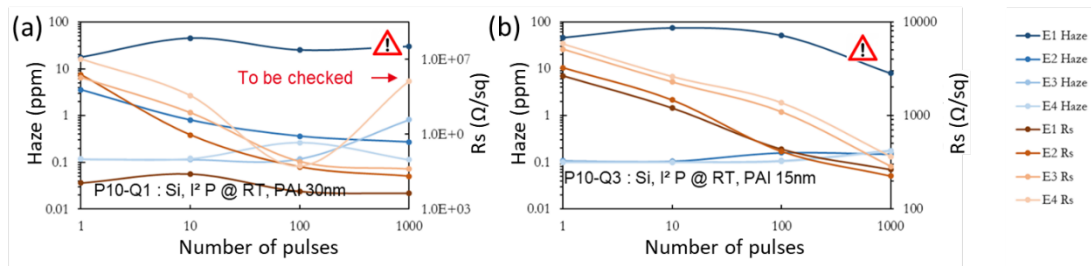

Figure 39: Haze and sheet resistance measurements as a function of number of pulses for (a) P10-Q1 (PAI 30 nm) and (b) P10-Q3 (PAI 15 nm) Si samples

Summary and Conclusions

In this deliverable, we reported the final results of our investigations about the impact of the wafer temperature on the residual damage remaining after an ion implantation process, as well as on the electrical activation of the implanted dopants.

In section 1, we presented the case of a "heated implant" of Arsenic in Silicon. For the sample implanted at 150°C, additional annealing at 700°C and 800°C does not drastically change the photoluminescence peaks compared to the initial anneal sequence. However, after additional annealing at 900°C, the peaks in the photoluminescence spectrum are different. The annealing at 900°C is therefore associated with an evolution of the defects responsible for the observed A1 and A2 PL peaks. TEM analyses clearly indicate that the annealing at 900°C causes a change in the population of dislocation loops. The TEM images are therefore consistent with the hypothesis of a link between the A1 and A2 peaks observed in photoluminescence and the presence of DLs. The decrease in density of the DLs is a classical effect after annealing and is explained by the Ostwald ripening mechanism. The nature of the DLs does not seem to change between the reference sample and the annealed samples (faulted dislocations). The

decrease in density of the DLs would be related to the change of the strain field. An in-depth analysis of the defects observed in TEM is underway to confirm this hypothesis. Other TEM analyses are planned, in particular to explain the photoluminescence spectra of the sample implanted at 500°C.

In the second section, we presented the results obtained from the dedicated SiGe wafers fabricated and laser annealed by CEA-LETI, specifically designed for tasks T2.1 and T2.2 of the project. In the case of non-preamorphised wafers, samples implanted with amorphizing conditions have the best electrical and morphological properties after laser annealing. The SPER induced during laser annealing on these samples results in lower sheet resistance and a less rough surface. The laser energy density should be chosen below $E_M - 10\%$ to avoid an ER phenomenon.

For preamorphised wafers, the 15 nm PAI samples are recrystallized using laser annealing. The 30 nm PAI samples do not reach a full SPER after laser annealing, resulting in poorer electrical characteristics. The fluence energy at $E_M - 5\%$ is likely to introduce an ER phenomenon in all cases (less visible in the B implanted SiGe samples).

Finally, a first attempt to compare simulations and experimental results was also presented for the Boron heated implantations in Si. The active Boron profiles predicted by the KMC do not seem to agree with the SRP measurements. The KMC simulations nevertheless allow to predict several trends observed experimentally such as the increase of the sheet resistance with the implantation temperature in the case of boron implantations, or the activation rate as a function of the number of pulses. The improvement of the simulation models in this case will be detailed in deliverable 2.6

References

[1] Cristiano, F, „Formation energies and relative stability of perfect and faulted dislocation loops in silicon ," *Journal of Applied Physics* Bd. 87, Nr. 12, p. 8420-8428, 2000

[2] P. K. Giri, „Photoluminescence signature of silicon interstitial cluster evolution from compact to extended structures in ion-implanted silicon," *Semiconductor science and technology 20.6,* p. 638, 2005.

[3] Y. Yu, „Photoluminescence evolution in self-ion-implanted and annealed silicon," *Chinese Physics B,* Bd. 18.11, p. 4906, 2009.

[4] Bonafos, C, „Ostwald ripening of end-of-range defects in silicon," *Journal of Applied Physics* Bd. 83, Nr. 6, p. 3008-3017, 1998

[5] Sentaurus Process of Synopsys with Advanced Calibration. Ver. S 2021.06. (2021). www.synopsys.com

[6] P.A. Schumann, JR. and E.E. Gardner Solid-State Electronics Pergamon Press 1969 Vol. 12, pp. 371-375

[7] R. G. Mazur, S. M. Ramey, C.L. Hartford, E. J. Hartford, M. Kouno, L. S. Tan, in AIP Conference Proceedings 449, Characterization and Metrology for ULSI Technology, D. G. Seiler, A. C. Diebold, W. M. Bullis, T. J. Shaffner, R. McDonald, E. J. Walters, p. 226, American Institute of Physics, New York, 1998.

[8] R. Daubriac, E. Scheid, H. Rizk, R. Monflier, S. Joblot, R. Beneyton, P. Acosta Alba, S. Kerdilès, F. Cristiano, "A differential Hall effect measurement method with sub-nanometre

resolution for active dopant concentration profiling in ultrathin doped Si1−xGex and Si layers", Beilstein J. Nanotechnol., 9, 1926–1939, 2018.

[9] G. Masetti, „Modeling of carrier mobility against carrier concentration in arsenic-, phosphorus-, and boron-doped silicon.," *IEEE Transactions on electron devices,* Bd. 30, Nr. 7, pp. 764-769, 1983.

[10] Aboy M, „Kinetics of large B clusters in crystalline and preamorphized silicon," *Journal of Applied Physics,* Bd. 110, Nr. 7, p. 073524, 2011.

[11] Dagaut. L, „Investigation of recrystallization and stress relaxation in nanosecond laser annealed Si1-xGex/Si epilayers," *Applied Surface Science,* Bd. 527, p. 146752, 2020.